Check for updates

Nanostructured spinel manganese cobalt ferrite for high-performance supercapacitors

Ayman E. Elkholy, [ID] [ac] F. El-Taib Heakal [ID] [b] and Nageh K. Allam [ID] *[c]

We report on the synthesis of manganese cobalt ferrite ($MnCoFeO_4$) nanoparticles *via* a simple one-pot co-precipitation method and their characterization through energy-dispersive spectroscopy (EDS), X-ray diffraction (XRD), high-resolution transmission electron microscopy (HR-TEM), Fourier transform infrared (FT-IR) spectroscopy and N_2 adsorption/desorption techniques. The $MnCoFeO_4$ supercapacitor showed the maximum specific capacitance of 675 F g^{-1} at a scan rate of 1 mV s^{-1}. Its energy and power densities were 18.85 W h kg^{-1} and 337.50 W kg^{-1}, respectively, at a current density of 1.5 A g^{-1}. The cyclic stability was scrutinized *via* galvanostatic charging/discharging (GCD) and electrochemical impedance spectroscopy (EIS). The degradation of the supercapacitive performance was only 7.14% after 1000 GCD cycles, indicating an excellent long-term stability. The equivalent series resistance (ESR) remained nearly constant even after 1000 GCD cycles.

1. Introduction

Nowadays, the worldwide community suffers from serious environmental problems arising from an excessive combustion of fossil fuels.[1] Consequently, many researchers have paid great attention to manipulate the clean and sustainable energy sources as well as efficient energy conversion and storage technologies.[2] Batteries and supercapacitors are the typical devices used for the storage of electrical energy. Both of these store electricity through electrochemical processes.[3] Compared to the batteries, the supercapacitors are characterized by higher power density, rapid charge/discharge, and long-life service. Despite the advantages of high power density and high cycle life of supercapacitors, their intrinsically low energy density (*i.e.* the amount of energy stored per unit weight) has limited them from widespread commercial applications in comparison to batteries. To this end, increasing their energy density requires an extensive research and development,[4,5] including the merge of batteries and supercapacitors.[6]

According to their active materials, supercapacitors (SCs) are classified into two main types: electrochemical double layer capacitors (DCs) and electrochemical pseudocapacitors (PCs).[7,8] The active material in the DCs is composed of carbonaceous (carbon-based) materials, such as activated carbon, graphite, and graphene. Energy is stored physically within a DC *via* charge accumulation across the electrode/electrolyte

interface.[8,9] As for PCs, the active material is primarily composed of a transition metal (TM) oxide, a TM nitride or a conducting polymer. Energy is stored electrochemically within a PC *via* the reversible interfacial redox reactions in TMs or *via* ion intercalation throughout the electrode in conducting polymers.[5,10,11] Due to the intrinsic low specific capacitance (C_{sp}) and low energy density stored in the current SCs, it is vital to explore new materials that simultaneously exhibit high C_{sp} as well as high conductivity.[4] TMs are characterized by being cost-effective and displaying multiple oxidation states[7] in addition to their fast and reversible faradaic redox reactions.[12] Therefore, TMs are engrossed as the electrode materials for supercapacitor applications because of their outstanding electrochemical performance.[13] In addition, TM oxides can provide a higher theoretical C_{sp} than that of the conventional carbon-based materials and a better electrochemical stability than that of the polymeric materials.[7] Among them, RuO_2 has been widely investigated as a promising candidate because of its better conductivity and high C_{sp}; however, it is limited by its high cost, rarity,[13,14] and toxicity.[15] Alternative inorganic electrode materials such as MnO_2,[16] Co_3O_4,[17] NiO,[18] V_2O_5/VO_4,[19] WO_3,[20] and Fe_2O_3 [21] have been intensively investigated in SC applications owing to their wide availability, chemical stability, mechanical strength, safety, and eco-friendliness.[15] Recently, ferrites as SC materials have been explored by researchers due to their various redox states, electrochemical stability as well as remarkable magnetic, catalytic, optical, and electrical properties.[22] Ferrite-based materials have been synthesized in diverse nanostructured forms, including nanoparticles,[23] nanotubes,[24] nanofibers,[20] nanowires,[25,26] nanorods,[10] nanoflakes,[17,27] nanomesh arrays,[14] nanosheets,[17] and hollow structures.[28] Ferrites can be synthesized *via* various synthesis techniques

[a] Department of Analysis and Evaluation, Egyptian Petroleum Research Institute, 11727 Cairo, Egypt

[b] Chemistry Department, Faculty of Science, Cairo University, 12613 Giza, Egypt

[c] Energy Materials Laboratory, School of Sciences and Engineering, The American University in Cairo, 11835 New Cairo, Egypt. E-mail: nageh.allam@aucegypt.edu

including sol–gel method,[12] co-precipitation method,[29] template method,[24] solvothermal method,[30] microwave-assisted method,[10,13] electrodeposition method,[27] chemical spray method,[15] spray-pyrolysis method[15] and hydrothermal method.[14] Among these techniques, the co-precipitation method provides a simple route for the one-pot synthesis and the reaction conditions are mild and simple.[13]

Usually, the general formula for a spinel is AB_2O_4, where A refers to a divalent metal ion (M^{2+}) and B refers to a trivalent metal ion (M^{3+}). In a normal spinel structure, the A ions occupy the tetrahedral sites and the B ions occupy the octahedral sites.[31] Spinel ferrites, MFe_2O_4 or $MM'FeO_4$ (where M or M' = Mn, Co, Ni, Zn, Cu, etc.), are fascinating materials owing to their impressive magnetic, electrical, and optical properties in addition to their ability to exhibit different redox states and electrochemical stability. In spinel ferrites, the divalent metal ion (M^{2+}) occupies the tetrahedral site and the trivalent metal ion (M'^{3+} or Fe^{3+}) occupies the octahedral position.[12] According to Bernard et al.[32] and Kulkarni,[33] Mn atoms in $MnCoFeO_4$ prefer to occupy the tetrahedral positions, while Co atoms prefer to occupy the octahedral sites. Besides, the valence states of Mn, Co, and Fe are majorly (+II), (+III), and (+III), respectively. In contrast, Martens[34] has studied the magneto-optical properties of $Mn_xCoFe_{2-x}O_4$ (where $x = 0$, 0.5, and 1.0) prepared using a conventional ceramic technology with a final sinter treatment in oxygen for 24 h at 1200–1300 °C and found that Mn has the oxidation state (+III) and occupied the octahedral sites, while Co, in the form of Co^{2+}, could occupy both octahedral and tetrahedral positions with the latter being more favorable. These observations were confirmed by two later studies based on submicron $Mn_xCoFe_{2-x}O_4$ spinel ferrites by Chassaing et al.[35] and Laarj and Kacim.[36] In both studies, $Mn_xCoFe_{2-x}O_4$ spinels were prepared from the oxalic precursors and subjected to annealing treatment between 600 °C and 700 °C.

Numerous binary TM ferrites have been investigated for supercapacitor applications such as $ZnFe_2O_4$,[17,30] $CoFe_2O_4$,[14] $MnFe_2O_4$,[37] $CuFe_2O_4$,[26] and $SnFe_2O_4$.[10] However, few research studies were carried out on ternary TM ferrites as the electrodes for supercapacitor applications as listed in Table 1.

Herein, $MnCoFeO_4$ was synthesized in the form of nano-particles via the co-precipitation method and characterized by EDS, XRD, TEM, FT-IR analyses, and N_2 adsorption/desorption. Its supercapacitive performance in 6 M KOH was investigated via cyclic voltammetry (CV) and galvanostatic charging/discharging (GCD). The cyclic stability was studied via GCD and electrochemical impedance spectroscopy (EIS). The

materials showed an exceptional C_{sp} as compared to the C_{sp} of those reported in the literature.

2. Experimental methods

2.1. Preparation of $MnCoFeO_4$

To obtain $MnCoFeO_4$, 0.005 mole of $MnCl_2 \cdot 4H_2O$ was dissolved in 50 ml deionized water, 0.005 mole of $CoCl_2 \cdot 6H_2O$ was dissolved in 50 ml deionized water, and 0.01 mole of anhydrous $FeCl_3$ was dissolved in 250 ml deionized water. The three solutions were mixed together with continuous stirring and kept at 65 °C until thermal equilibrium was achieved. Then, 100 ml of 0.8 M NaOH solution was added dropwise to the mixed solution with continuous stirring and a black precipitate was formed. The formed precipitate was separated from the liquid phase and washed several times with deionized water via centrifugation until neutrality. The neutrality of the decanted aliquot was checked using phenolphthalein indicator. Finally, the washed precipitate was dried at 100 °C.

2.2. Characterization of $MnCoFeO_4$

Elemental composition was identified by means of energy-dispersive spectroscopy (EDS) using an Oxford EDS detector. The structural characteristics of the prepared material were investigated via X-ray diffraction (XRD) using a PANalytical X'pert PRO diffractometer with a Cu Kα radiation. The particle morphology of the prepared material was studied via high-resolution transmission electron microscopy (HR-TEM) using a JEOL JEM-2100 (Japan) electron microscope, operating at an accelerated voltage of 200 keV. Prior to the analysis, the sample was dispersed in ethanol using a probe sonicator and then a drop of the much-diluted sample solution was deposited on a carbon-coated copper grid and allowed to be evaporated at room temperature. Fourier transform infrared (FT-IR) spectroscopy was performed in the range of 400–4000 cm^{-1} to determine the metal oxide peaks using a PerkinElmer Spectrum One spectrophotometer. The adsorption capability of the prepared material and its specific surface area were investigated by N_2 gas adsorption/desorption (at 77 K) and Brunauer–Emmett–Teller (BET) analysis, respectively, using a Quantachrome NOVA Station A (version 11.03).

2.3. Electrochemical measurements

A working electrode was prepared using a homogenous slurry of $MnCoFeO_4$ with carbon black acting as a conductive additive

Table 1 Supercapacitive performance of $MnCoFeO_4$ compared with some other ferrite-based materials

Material	C_{sp} (F g^{-1})	ED (W h kg^{-1})	PD (W kg^{-1})	Ref.
$CuCoFe_2O_4$	76.9	7.90	1711.95	12
$NiCoFe_2O_4$	50.0	4.79	1426.23	12
$NiCuFe_2O_4$	44.0	4.62	1001.99	12
$CuCoFe_2O_4$	397.0	3.53	198.50	49
$Al_xCu_yCo_2Fe_2O_4$ ($x + y + z = 1$)	256.0–540.0	0.58–8.42	128.00–270.00	49
$MnCoFeO_4$	**670.0**	**3.15**	**2250.00**	**This work**

and poly(vinylidene difluoride) acting as a binder in a DMF solvent with a weight ratio of 70 : 20 : 10. The prepared slurry was stirred for about 48 h at room temperature, then coated onto a part of a 1 cm × 2 cm chip of nickel foam (as a supporter and current collector) and dried at 60 °C. The supercapacitive performance of the prepared $MnCoFeO_4$ electrode was investigated using a three-electrode cell containing the working electrode (the prepared electrode under study), a counter electrode (a Pt coil) and a reference electrode (a saturated calomel electrode, SCE) in a 6 M KOH solution at room temperature. The electrochemical measurements involved cyclic voltammetry (CV), galvanostatic charging/discharging (GCD), and electrochemical impedance spectroscopy (EIS) using the electrochemical workstation (CHI 760D, CH Instruments, U.S.A.). CV measurements were performed within the potential window of 0–0.45 V at different scan rates (from 1 to 100 mV s^{-1}). GCD measurements were carried out at different current densities (1.5–10 A g^{-1}) within the same potential window. The EIS measurements were performed in the frequency range of 100 kHz to 0.1 Hz at the steady-state open circuit potential (0.261 V *vs.* SCE) with a sinusoidal perturbation amplitude of 10 mV. EIS parameters were derived using EC-Lab V10.40 software.

The specific capacitance (C_{sp}, F g^{-1}) was then calculated from data obtained from CV and GCD measurements according to eqn (1)[10,22] and (2)[14,17,38] respectively.

$$C_{sp} = \frac{\int I(\mathrm{d}V)}{mv\Delta V} \tag{1}$$

$$C_{sp} = \frac{I\Delta t}{m\Delta V} \tag{2}$$

where I is the response current (A), m is the mass of active material (g), v is the scan rate (mV s^{-1}), ΔV is the potential window (V), and Δt is the discharge time (s). The coulombic efficiency (η) was calculated from GCD measurements as follows:[39,40]

$$\eta = \frac{t_d}{t_c} \times 100 \tag{3}$$

where t_c and t_d are the times of charging and discharging with the same current density, respectively. The energy density and the power density of the $MnCoFeO_4$ supercapacitor can be calculated from eqn (5) and (6)[14,40–42]

$$E = \frac{1}{2}C_{sp}\Delta V^2 \tag{4}$$

eqn (4) can be reformed as follows:

$$E = \frac{1}{2}\frac{I\Delta Vt}{m} \tag{5}$$

$$P = \frac{E}{t} \tag{6}$$

where I is the response current (A), m is the mass of active material (kg), ΔV is the potential window (V), and t is the discharge time (h).

3. Results and discussion

3.1. Material characterization

Fig. 1a demonstrates the EDS spectrum of the prepared $MnCoFeO_4$, showing the peaks of Mn, Co, Fe, and O elements. The presence of these elements in the formed precipitate confirmed that Mn, Co, and Fe have co-precipitated simultaneously in the oxide form. The elemental composition obtained from EDS analysis reveals that the atomic percentages of Mn, Co, Fe, and O are 10.14%, 9.81%, 18.75%, and 61.30%, respectively. As a result, their atomic ratio is approximately 1 : 1 : 2 : 6. Fig. 1b shows the XRD pattern of the prepared material. All diffraction peaks are coincident to the Miller
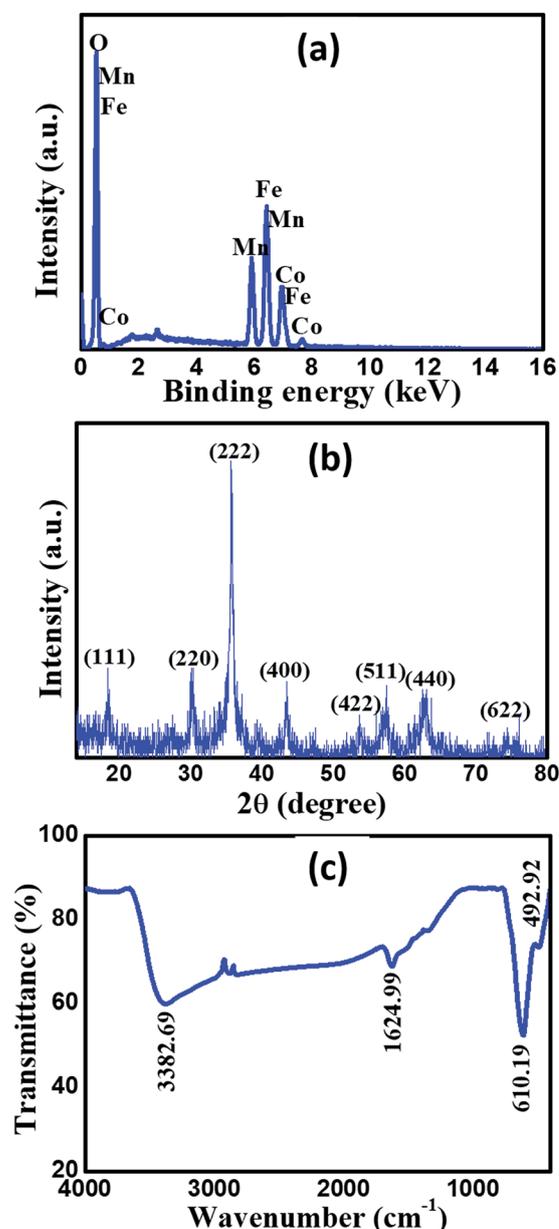

Fig. 1 (a) EDS spectrum, (b) XRD pattern, and (c) FT-IR spectrum for the as-prepared $MnCoFeO_4$.

indices (111), (220), (222), (400), (422), (511), (440) and (622) of the standard data for $MnCoFeO_4$ (cubic, space group: $Fd\bar{3}m$, ICDD card number: 04-010-1895), which confirms the formation of $MnCoFeO_4$ with the spinel structure. Fig. 1c displays the FT-IR spectrum of $MnCoFeO_4$ recorded in the frequency range 4000–400 cm^{-1}. The lower-frequency band (493 cm^{-1}) is assigned to the octahedral groups ([Fe^{3+}–O^{2-}] and [Mn^{3+}–O^{2-}]), while the higher-frequency band (610 cm^{-1}) is assigned to the stretching of the tetrahedral groups ([Co^{2+}–O^{2-}]) present in the spinel ferrite.[12] The FT-IR absorption bands appearing at 3383 cm^{-1} and 1625 cm^{-1} are referred to adsorbed water molecules.[41]

Fig. 2 shows the HR-TEM images of the as-fabricated $MnCoFeO_4$, indicating the formation of nanoparticles with sizes ranging *ca.* 30–40 nm. Fig. 3a shows the N_2 adsorption/desorption isotherm for the as-synthesized $MnCoFeO_4$. According to the IUPAC classification of gas adsorption/desorption isotherms,[43] the obtained N_2 adsorption/desorption isotherm is of type IV, which is characteristic to the mesoporous materials. The characteristic feature of this isotherm is its hysteresis loop, which arises when the adsorption and desorption curves do not coincide and is associated with the capillary condensation taking place in the mesopores. Moreover, the initial part, where adsorption/desorption curves are coincident, is attributed to the monolayer-multilayer adsorption. These features confirm the mesoporous structure of the prepared $MnCoFeO_4$. It is worth mentioning that porous materials are generally classified according to their pore diameter (d) into three categories: macroporous ($d > 50$ nm), mesoporous ($d = 2$–50 nm), and microporous materials ($d < 2$ nm).[5] Fig. 3b shows the pore diameter distribution curve obtained by the Barrett–Joyner–Halenda (BJH) method using the desorption branch of the nitrogen isotherm.[17] It reveals an average pore diameter of 10.036 nm. The BET method likely yields a value of actual surface area if the isotherm is either of type II or type IV.[43] Hence, the surface area obtained from multipoint BET is noted to be 104.963 m^2 g^{-1}.

3.2. Electrochemical characterization

3.2.1. Specific capacitance.
The electrochemical capacitive performance of the as-fabricated $MnCoFeO_4$ was examined *via* CV and GCD measurements. The CV curves of $MnCoFeO_4$ were recorded at different scan rates in the potential range of 0–0.45 V_{SCE} in 6 M KOH (Fig. 4a). The CV curves show faradic-type capacitive features, where two peaks appear at ~0.38 V and ~0.19 V for the oxidation and reduction processes, respectively. The specific capacitance (C_{sp}) obtained from CV measurements is dependent on the scan rate, where the peak current density (I_p, A g^{-1}) of $MnCoFeO_4$ clearly increases as a function of scan rate. The maximum C_{sp} (675 F g^{-1}) is obtained at the slowest scan rate (1 mV s^{-1}), while C_{sp} calculated at 100 mV s^{-1} is 238.81 F g^{-1} (the inset of Fig. 4a). This could be attributed to the existence of a large Ohmic resistance at large scan rates.[37] In addition, the electrolyte ions do not have a sufficient time, at high rates of potential scanning, to entirely diffuse through the electrode nanopores wherever the faradaic reactions occur.[8] Also, this behavior suggests that there are parts of the electrode surface inaccessible at high rates of charging/discharging.[44] Therefore, electrical energy is electrochemically stored in an efficient manner in the $MnCoFeO_4$ supercapacitor at a slower scan rate.

Moreover, Fig. 4a demonstrates the pairs of distinct and broad redox peaks corresponding to the redox transitions of Co^{3+}/Co^{2+} and Mn^{3+}/Mn^{2+}. The redox peaks of Co^{3+}/Co^{2+} and Mn^{3+}/Mn^{2+} seem to be merging together because their standard electrode potentials are comparable (1.92 and 1.50 V_{NHE}, respectively[45]). The probable processes associated with the capacitive behavior of $MnCoFeO_4$ can be related to the presence of two redox systems. The redox reactions related to both systems could proceed according to eqn (7)[46] and (8)[42], respectively.
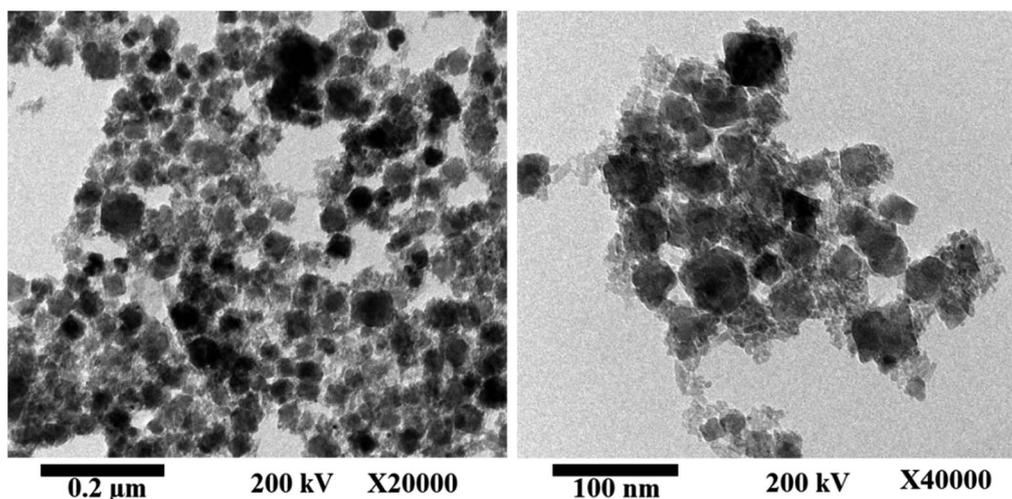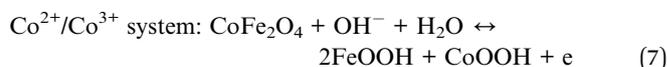
Co^{2+}/Co^{3+} system: $CoFe_2O_4 + OH^- + H_2O \leftrightarrow$
$$2FeOOH + CoOOH + e \qquad (7)$$

Fig. 2 HR-TEM images of the as-prepared $MnCoFeO_4$.
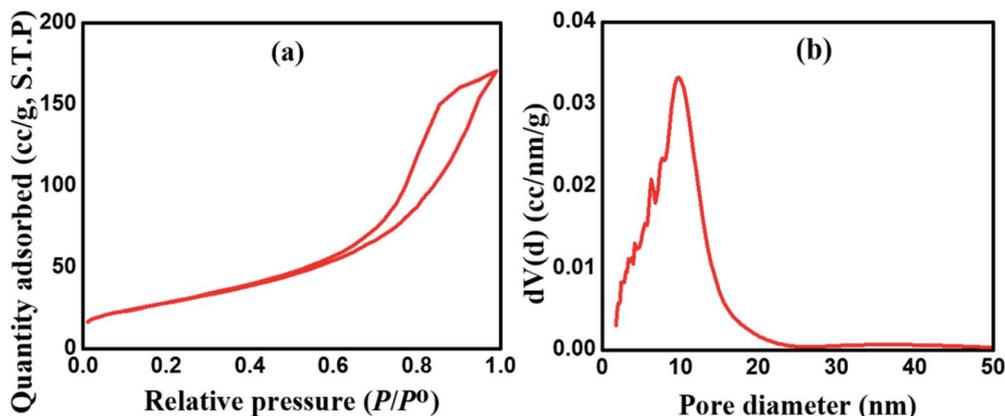
Fig. 3 (a) N_2 adsorption/desorption isotherm and (b) BJH pore size distribution for the as-prepared $MnCoFeO_4$.
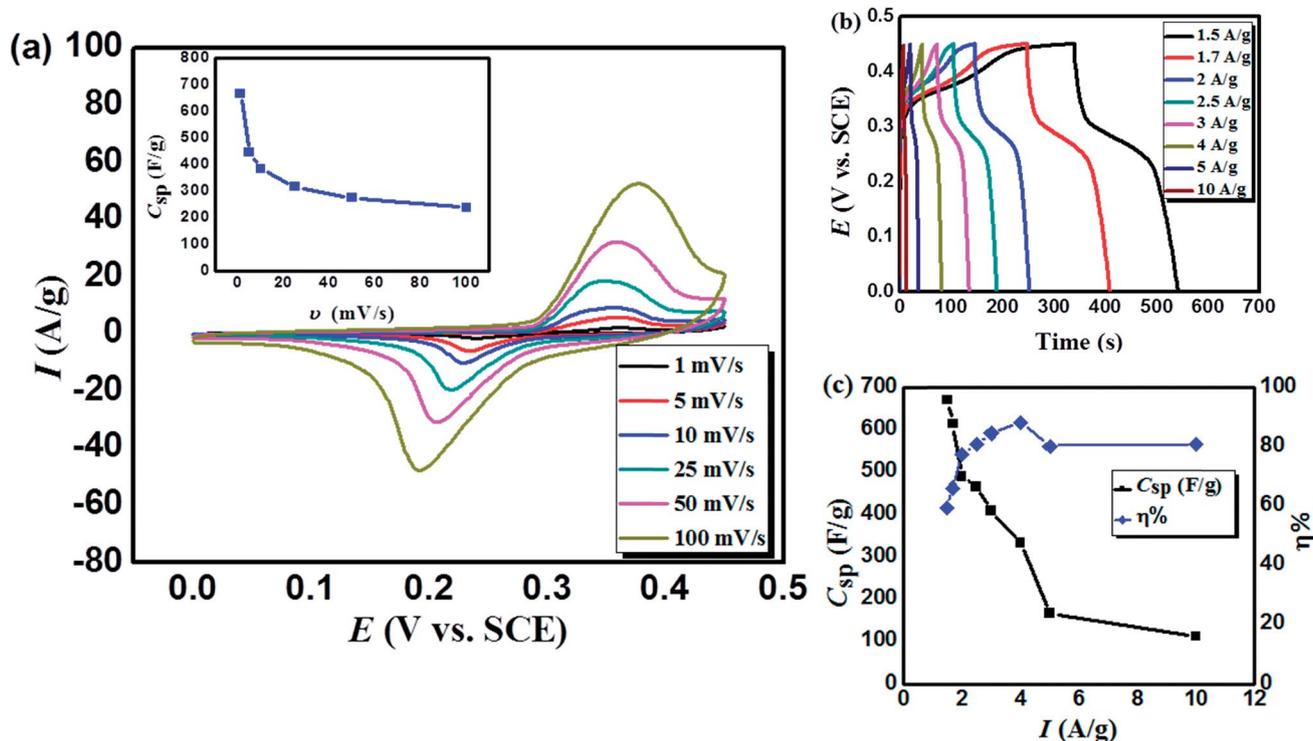

Fig. 4 (a) CV curves recorded for as-prepared $MnCoFeO_4$ at different scan rates in the potential range of $0-0.45$ V_{SCE} in the 6 M KOH electrolyte and the inset shows the dependence of the specific capacitance on the scan rate, (b) Galvanostatic charge/discharge curves recorded for $MnCoFeO_4$, and (c) the calculated C_{sp} and $\eta\%$ at different current densities in the potential range of $0-0.45$ V_{SCE} in the 6 M KOH electrolyte.

Mn^{2+}/Mn^{3+} system: $MnFe_2O_4 + OH^- + H_2O \leftrightarrow$

$$2FeOOH + MnOOH + e \quad (8)$$
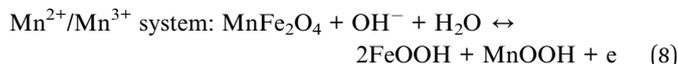
The CV profiles (at different scan rates) demonstrate the same behavior, revealing the reversibility of the redox reactions. In addition, with the increase in the scan rate, both oxidation and reduction peaks shift towards more anodic and cathodic directions, respectively. For example, upon increasing the scan rate from 1 to 100 mV s^{-1}, the anodic peak potential ($E_{p,a}$) increased from 0.358 to 0.378 V_{SCE}, while the anodic peak current ($I_{p,a}$) increased from 2.063 to 52.494 (A g^{-1}). This effect

results from the unavoidable overpotential due to the increase in the internal diffusion resistance and I_p increases with υ due to the fast interfacial kinetics.[14]

Galvanostatic charge/discharge (GCD) measurement is an accurate technique for determining the electrochemical performance of supercapacitors particularly for those based on pseudo-capacitance.[40] Fig. 4b displays the GCD curves recorded for $MnCoFeO_4$ in 6 M KOH. Unlike the GCD curves of carbon-based materials exhibiting a semi-triangular shape, where their capacitances are mainly attributed to a pure electric double layer capacitance, the GCD curves of $MnCoFeO_4$ show

deviations from linearity due to its pseudocapacitive nature.[22,47] Clearly, the MnCoFeO$_4$ electrode demonstrates higher charging and discharging times as the current density decreases, resulting in higher values of specific capacitance (Fig. 4c). For example, on decreasing the current density from 10 A g^{-1} to 1.5 A g^{-1}, C_{sp} increases from 112 to 670 F g^{-1}. Furthermore, the columbic efficiency ($\eta\%$) increases with the current density up to 89% at 4 A g^{-1}, after which it becomes constant ($\sim$81%).
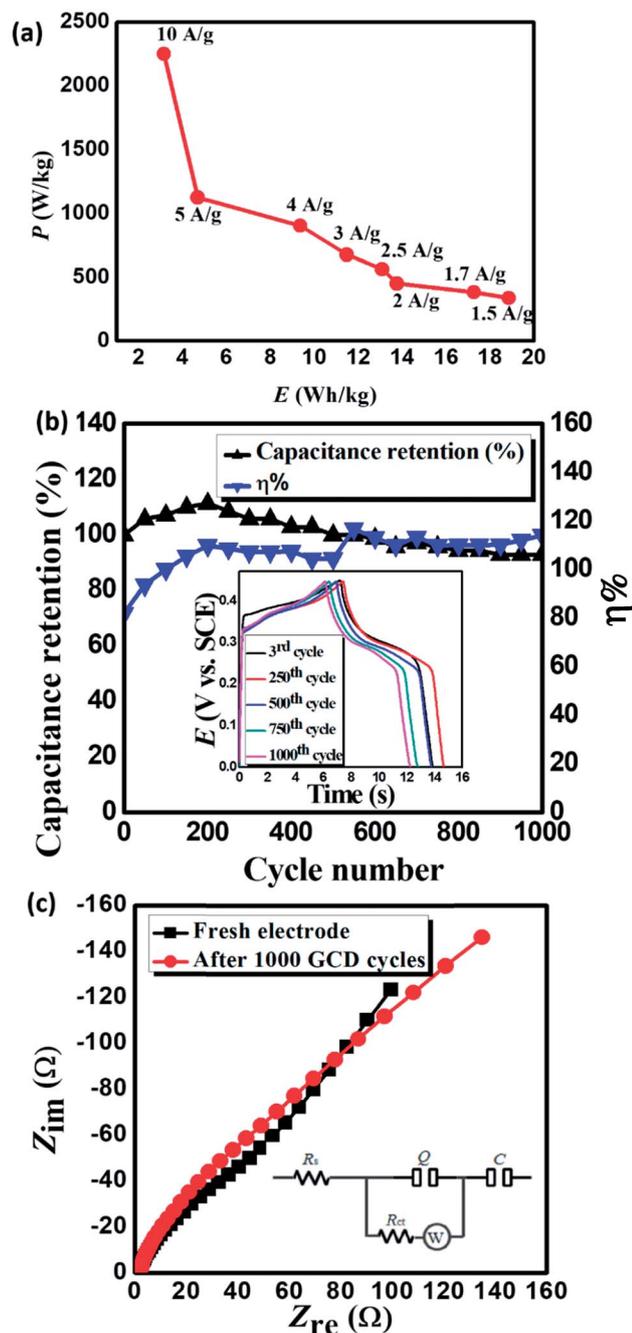

Fig. 5 (a) Ragone plot, (b) cycling stability curves, and (c) Nyquist spectra recorded for MnCoFeO$_4$ before and after 1000 galvanostatic charge/discharge (GCD) cycles.

Power density (PD) and energy density (ED) are two important parameters for the evaluation of the electrochemical performance of supercapacitors and electrode materials.[40] Fig. 5a displays the Ragone plot of MnCoFeO$_4$ obtained from GCD measurements[48] with the current densities ranging from 1.5 to 10 A g^{-1}. Fig. 5a demonstrates that the ED stored in MnCoFeO$_4$ and its corresponding PD (at a current density of 1.5 A g^{-1}) are 18.85 W h kg^{-1} and 337.50 W kg^{-1}, respectively. On the other hand, at a current density of 10 A g^{-1}, ED and PD values are 3.15 W h kg^{-1} and 2250.00 W kg^{-1}, respectively. Table 1 depicts the supercapacitive performance parameters, including C_{sp}, PD, and ED for MnCoFeO$_4$ and some ternary and quaternary TM ferrites. It should be noted that MnCoFeO$_4$ has an excellent C_{sp} and PD in comparison to those of the previously investigated materials.

3.2.2. Cycling stability. Cycling stability is another important factor that determines the efficiency and durability of supercapacitors,[37] which can be expressed in terms of capacitance retention (%) and coulombic efficiency ($\eta\%$).[40] Fig. 5b illustrates the capacitance retention (%) and $\eta\%$ of the prepared supercapacitor recorded during 1000 continuous GCD cycles at a high current density (10 A g^{-1}). The capacitance retention (%) increases up to 200 cycles and reaches 111.43%. Following this, it starts to decrease and reaches $\sim$92.86% after 1000 GCD cycles, indicating an excellent long-term stability. In addition, the coulombic efficiency increases with time and reaches 114% after 1000 GCD cycles. The excellent stability of MnCoFeO$_4$ could be attributed to the synergistic effects of the three transition metals.

EIS is a powerful tool used to investigate the features of an electrode/electrolyte interface as supercapacitors by evaluating the frequency behavior and equivalent series resistance (ESR).[37] EIS offers information about the internal resistance of the electrode material and the resistance between the electrode and the electrolyte.[40] EIS spectra (Fig. 5c) display a depressed semicircle in the high-frequency region linked to an inclined straight line in the low-frequency region. The slope of the inclined line is decreased after 1000 GCD cycles. The equivalent circuit used to analyze EIS spectra is depicted in the inset of Fig. 5c.[48]

The time constant ($QR_{ct}W$) represents the depressed semicircle in the high-frequency region, where R_{ct} is the charge-transfer resistance caused by the faradaic process and Q is a constant phase element representing the non-ideal double-

Table 2 EIS parameters calculated for the MnCoFeO$_4$ electrode before and after 1000 cycles GCD

	Fresh electrode	After 1000 cycles
R_s (Ω)	1.74	1.76
Q (mF)	2.68	2.57
n	0.86	0.87
R_{ct} (Ω)	53.37	78.74
W (Ω s$^{-0.5}$)	59.67	101.90
C (mF)	35.10	84.90

layer capacitance. Table 2 reveals that R_s, representing the ESR, remains nearly constant even after 1000 GCD cycles. The ESR includes electrolyte resistance, internal resistance of the electrode and contact resistance between the electrode and the current collector.[5] R_{ct} suffers a slight increase from 53.37 Ω to 78.74 Ω, indicating that the amount of charge stored in this material is slightly decreased. The linear part of the curve is inclined by ∼45°, indicating Warburg impedance (W) that is related to the frequency-dependent diffusion resistance of electrolyte ions.[15,17,47] The value of W increases from 59.67 Ω s$^{-0.5}$ to 101.90 Ω s$^{-0.5}$, indicating a slowdown in the diffusion rate due to a somewhat difficult penetration of electrolyte ions through the electrode mesopores with long-term use.

4. Conclusions

Mesoporous MnCoFeO$_4$ nanoparticles, with diameters in the range 30–40 nm, were successfully synthesized via a one-pot simple co-precipitation method without annealing as confirmed by the TEM analysis. The XRD results confirmed the spinel structure of the fabricated MnCoFeO$_4$ nanoparticles. The BJH average pore diameter was found to be 10.036 nm and the BET surface area was 104.963 m^2 g^{-1}. The as-prepared MnCoFeO$_4$ material was evaluated as a supercapacitor electrode in 6 M KOH using CV and GCD measurements. The maximum C_{sp} calculated from CV measurement was 675 F g^{-1} at a scan rate of 1 mV s^{-1} and that calculated from GCD measurement was 670 F g^{-1} at a current density of 1.5 A g^{-1}. The energy and power densities of the MnCoFeO$_4$ supercapacitor were 18.85 Wh kg^{-1} and 337.50 W kg^{-1}, respectively at a current density of 1.5 A g^{-1}. The cyclic stability was scrutinized via GCD and EIS. The capacitance retention (%) was 111.43% and 92.86% after 200 and 1000 GCD cycles, respectively, indicating an excellent long-term stability. The equivalent series resistance (ESR) remained nearly the same even after 1000 GCD cycles.

Conflicts of interest

There are no conflicts to declare.

Acknowledgements

Notes and references

1 E. M. Gabr, S. M. Mohamed, S. A. El-Temtamy and T. S. Gendy, Egypt. J. Pet., 2016, 25, 65–74.

2 L. Hao, X. Li and L. Zhi, Adv. Mater., 2013, 25, 3899–3904.

3 C. Liu, F. Li, L. P. Ma and H. M. Cheng, Adv. Mater., 2010, 22, E28–E62.

4 N. Choudhary, C. Li, J. Moore, N. Nagaiah, L. Zhai, Y. Jung and J. Thomas, Adv. Mater., 2017, 29, 1605336.

5 A. Yu, V. Chabot and J. Zhang, Electrochemical supercapacitors for energy storage and delivery: fundamentals and applications, CRC Press, New York, 2013.

6 F. Béguin, V. Presser, A. Balducci and E. Frackowiak, Adv. Mater., 2014, 26, 2219–2251.

7 D. Chen, Q. Wang, R. Wang and G. Shen, J. Mater. Chem. A, 2015, 3, 10158–10173.

8 D. M. El-Gendy, N. A. A. Ghany, E. F. El Sherbini and N. K. Allam, Sci. Rep., 2017, 7, DOI: 10.1038/srep43104.

9 S. Faraji and F. N. Ani, Renewable Sustainable Energy Rev., 2015, 42, 823–834.

10 K. Bindu, K. Sridharan, K. M. Ajith, H. N. Lim and H. S. Nagaraja, Electrochim. Acta, 2016, 217, 139–149.

11 D. Ham, J. Chang, S. H. Pathan, W. Y. Kim, R. S. Mane, B. N. Pawar, O.-S. Joo, H. Chung, M.-Y. Yoon and S.-H. Han, Curr. Appl. Phys., 2009, 9, S98–S100.

12 B. Bhujun, M. T. T. Tan and A. S. Shanmugam, Results Phys., 2017, 7, 345–353.

13 Y. Zhang, L. Li, H. Su, W. Huang and X. Dong, J. Mater. Chem. A, 2015, 3, 43–59.

14 L. Liu, H. Zhang, Y. Mu, Y. Bai and Y. Wang, J. Power Sources, 2016, 327, 599–609.

15 M. K. Zate, S. M. F. Shaikh, V. V. Jadhav, K. K. Tehare, S. S. Kolekar, R. S. Mane, M. Naushad, B. N. Pawar and K. N. Hui, J. Anal. Appl. Pyrolysis, 2015, 116, 177–182.

16 Y. Zhang, Q.-q. Yao, H.-l. Gao, L.-s. Zhang, L.-z. Wang, A.-q. Zhang, Y.-h. Song and L.-x. Wang, J. Anal. Appl. Pyrolysis, 2015, 111, 233–237.

17 M. M. Vadiyar, S. S. Kolekar, J.-Y. Chang, A. A. Kashale and A. V. Ghule, Electrochim. Acta, 2016, 222, 1604–1615.

18 S. Navale, V. Mali, S. Pawar, R. Mane, M. Naushad, F. Stadler and V. Patil, RSC Adv., 2015, 5, 51961–51965.

19 H. Wu and K. Lian, J. Power Sources, 2014, 271, 534–537.

20 J. Xu, T. Ding, J. Wang, J. Zhang, S. Wang, C. Chen, Y. Fang, Z. Wu, K. Huo and J. Dai, Electrochim. Acta, 2015, 174, 728–734.

21 B. Lokhande, R. Ambare and S. Bharadwaj, Measurement, 2014, 47, 427–432.

22 P. Xiong, H. Huang and X. Wang, J. Power Sources, 2014, 245, 937–946.

23 A. Shanmugavani, D. Kalpana and R. K. Selvan, Mater. Res. Bull., 2015, 71, 133–141.

24 Y. Xu, J. Wei, J. Yao, J. Fu and D. Xue, Mater. Lett., 2008, 62, 1403–1405.

25 Y. Asano, K. Nakaoka, K. Murashiro, T. Komatsu and K. Hoshino, Mater. Lett., 2012, 81, 162–164.

26 S. Giri, D. Ghosh, A. P. Kharitonov and C. K. Das, Funct. Mater. Lett., 2012, 05, 1250046.

27 V. V. Jadhav, M. K. Zate, S. Liu, M. Naushad, R. S. Mane, K. N. Hui and S.-H. Han, Appl. Nanosci., 2016, 6, 511–519.

28 M. Li, W. Xu, W. Wang, Y. Liu, B. Cui and X. Guo, J. Power Sources, 2014, 248, 465–473.

29 X.-q. Bao, J. Zhu, X.-x. Gao, Y. Qiao and S.-z. Zhou, J. Magn. Magn. Mater., 2009, 321, 1832–1837.

30 M. Zhu, X. Zhang, Y. Zhou, C. Zhuo, J. Huang and S. Li, RSC Adv., 2015, 5, 39270–39277.

31 P. R. Graves, C. Johnston and J. J. Campaniello, *Mater. Res. Bull.*, 1988, **23**, 1651–1660.

32 J.-L. Bernard, N. Baffier and M. Huber, *J. Solid State Chem.*, 1973, **8**, 50–56.

33 D. Kulkarni, *Curr. Sci.*, 1974, **43**, 374–375.

34 J. Martens, *J. Appl. Phys.*, 1986, **59**, 3820–3823.

35 I. Chassaing, L. Presmanes, P. Tailhades and A. Rousset, *Solid State Ionics*, 1992, **58**, 261–267.

36 M. Laarj, S. Kacim and B. Gillot, *J. Solid State Chem.*, 1996, **125**, 67–74.

37 P. Guo, Z. Li, S. Liu, J. Xue, G. Wu, H. Li and X. S. Zhao, *J. Mater. Sci.*, 2017, **52**, 5359–5365.

38 Z. Wang, W. Jia, M. Jiang, C. Chen and Y. Li, *Nano Res.*, 2016, **9**, 2026–2033.

39 A. Rai, A. L. Sharma and A. K. Thakur, *Solid State Ionics*, 2014, **262**, 230–233.

40 W. Wang, Q. Hao, W. Lei, X. Xia and X. Wang, *J. Power Sources*, 2014, **269**, 250–259.

41 M. A. Mousa, M. Khairy and M. Shehab, *J. Solid State Electrochem.*, 2017, **21**, 995–1005.

42 P. Xiong, C. Hu, Y. Fan, W. Zhang, J. Zhu and X. Wang, *J. Power Sources*, 2014, **266**, 384–392.

43 K. S. Sing, *Pure Appl. Chem.*, 1985, **57**, 603–619.

44 D. K. Pawar, S. M. Pawar, P. S. Patil and S. S. Kolekar, *J. Alloys Compd.*, 2011, **509**, 3587–3591.

45 M. D. Arning and S. D. Minteer, in *Handbook of Electrochemistry*, Elsevier, 2007.

46 J. Hao, W. Yang, Z. Zhang, B. Lu, B. Zhang and J. Tang, *Electrochim. Acta*, 2015, **152**, 13–18.

47 H. Che, A. Liu, J. Mu, C. Wu and X. Zhang, *Ceram. Int.*, 2016, **42**, 2416–2424.

48 S. G. Mohamed, S. Y. Attia and N. K. Allam, *Mater. Today Energ.*, 2017, **4**, 97–104.

49 B. Bhujun, M. T. T. Tan and A. S. Shanmugam, *Ceram. Int.*, 2016, **42**, 6457–6466.